# Stochastic Black Start Resource Allocation to Enable Dynamic Formation of Networked Microgrids and DER-Aided Restoration

Cong Bai, *Graduate Student Member, IEEE*, Salish Maharjan, *Member, IEEE*, Han Wang,
and Zhaoyu Wang, *Senior Member, IEEE*

***Abstract*—Extended outages in distribution systems (DSs) dominated by distributed energy resources (DERs) require innovative black start (BS) strategies to ensure efficient and secure restoration. This paper proposes a two-stage stochastic resource allocation method within synchronizing dynamic microgrids for black start (SDMG-BS), enabling risk-averse and adaptive restoration across diverse scenarios while maintaining frequency security. Virtual synchronous generator (VSG)-controlled grid-forming inverters (GFMIs) with primary frequency governors are modeled as BS sources, with frequency response constrained by three transient indices to ensure stability during load pick-up. SDMG-BS enables location-independent synchronization among restored microgrids and the transmission grid (TG) via smart switches (SSWs). A scenario-based stochastic programming model addresses multi-source uncertainties, including seasonal variations in renewable output, load demand, and TG outage duration. The linear frequency model used in planning is validated to exceed 90% accuracy. Case studies on a modified IEEE 123-node feeder demonstrate that the proposed approach restores up to 20% more critical load than deterministic baselines, executes two MG synchronizations prior to TG reconnection, and maintains all transient frequency indices within safe bounds across all scenarios. The results highlight the effectiveness of SDMG-BS in enhancing resilience and operational flexibility under uncertainty.**

***Index Terms*—Black start, resource allocation, dynamic microgrids, synchronization, frequency security, stochastic optimization.**

## I. INTRODUCTION

FREQUENT transmission grid (TG) failures caused by severe weather and cyberattacks have led to an increasing number of blackouts in downstream distribution systems (DSs) [1]. As a result, the self-start capability of DSs supported by the black start (BS) technique is essential for managing outages and enhancing the system's resilience without relying on external resources. However, the traditionally used BS power sources, such as diesel generators (DGs), are costly, necessitating a novel and efficient BS strategy for modern distributed energy resource (DER)-led DSs [2], [3].

Despite the growing interest in DER-led BS strategies, three critical gaps motivate this work. First, the dynamic frequency performance of DERs, particularly grid-forming inverters (GFMIs), is often oversimplified or overlooked in existing BS models, undermining the accuracy of frequency stability assessments during restoration [4], [5], [6]. Second, current methods lack the flexibility to dynamically form microgrids (MGs) throughout the restoration process [7]. While some studies attempt to model MG evolution, their approaches heavily depend on the fixed locations of black-start-capable sources, which limits their integration into comprehensive planning models [8], [9]. Third, the impact of key uncertainties—such as fluctuating DER output and the unpredictable availability of the TG—remains underexplored in BS resource allocation, potentially reducing the resilience of restoration strategies [10], [11], [12].

BS resource allocation involves optimally placing and sizing resources that can restore the DS while ensuring security and efficiency [10], [13]. Unlike traditional methods that rely solely on DGs, DER-based BS strategies integrate diverse resources for rapid and comprehensive system recovery. Renewable energy sources (RESs), such as photovoltaic (PV) systems and wind turbines (WTs), are typically connected to the grid through grid-following inverters (GFLIs), which lack self-start capability [14]. To energize these RESs and leverage them for restoration, DSs utilize battery energy storage systems (BESSs) with GFMIs to form MGs during the recovery process [15]. The optimal location and sizing of GFMI-based BESSs are crucial for effective BS strategies. Additionally, advancements in communication and control technologies have led to the development of smart switches (SSWs) capable of dynamic reconfiguration, further enhancing the flexibility of DER-based BS strategies [16].

Several efforts have been made to model the frequency dynamics of DERs during restoration. A two-level BS framework is proposed in [4], where a 7-th-order transient simulation model for the GFMI-based DER is created to address frequency stability. However, this approach requires support from a dynamic

---

Received 2 January 2025; revised 14 July 2025; accepted 14 September 2025. This work was supported in part by the National Science Foundation through ECCS under Grant 2042314, in part by Power System Engineering and Research Center (PSERC) under Grant S-110, and in part by the U.S. Department of Energy Solar Energy Technologies Office under Agreement 40385. Paper no. TPWRS-00005-2025.

The authors are with the Department of Electrical and Computer Engineering, Iowa State University, Ames, IA 50011 USA (e-mail: congbai@iastate.edu; salish@iastate.edu; hanwang6@iastate.edu; wzy@iastate.edu).

Color versions of one or more figures in this article are available at https://doi.org/10.1109/TPWRS.2025.3611389.

Digital Object Identifier 10.1109/TPWRS.2025.3611389

simulation model to estimate the frequency nadir, which can be computationally complex for long-term planning problems like BS resource allocation. Additionally, it overlooks the rate of Change of Frequency (RoCoF). Similarly, a simulation-assisted service restoration model is presented in [5], where a droop-based controller for the GFMI-based DER is adopted to deal with the frequency fluctuations during the BS. To handle the restoration of a low inertia power system, a fast frequency response enabled bi-level optimization model is established in [6], where the RoCoF and the frequency nadir limit the maximum imbalanced power of the system. This model does not put constraints on frequency directly while the quasi-steady frequency regulation of DER is neglected. To fully utilize the potential of GFMI-based DER and overcome significant frequency variations during the BS, a comprehensive dynamic model that includes multiple transient indices is currently lacking in the literature.

Beyond frequency dynamics, synchronization among restored MGs and with the TG is another critical aspect of BS operations. Many existing works [4], [5], [6], [7] form isolated MGs at the end of the restoration process, but their continuous operation is questionable when relying solely on DER-based BS and restoration. A frequency-based synchronization is necessary for the continuous operation of MGs supported by DERs. A reactive power synchronization method for BS supported by PV systems is proposed in [17] to avoid the impact of active power variations on synchronism. However, this method restricts the optimization of synchronization during BS. To mitigate the inrush energization current and supply a smooth synchronization with neighboring MGs, a modified virtual synchronous generator (VSG) controller is designed for GFMI-based DERs in [18], validated in a real-time platform. Still, this method prohibits the assistance between the restored MGs and only relies on a fixed synchronization scheme after the entire system is energized. Pioneering works in [8], [9] have proposed efficient BS strategies for the DS, where the dynamic boundaries for networked MGs allow synchronization during the restoration. However, these studies depend on the location of MGs and the structure of DS, which restricts the flexibility of the choice of BS path. A more elastic synchronizable BS method is needed to find optimal cranking paths for BS at the resource allocation stage that considers the location and size of GFMIs as a decision variable.

Existing BS resource allocation models often employ deterministic approaches, failing to address uncertainties such as varying RES output, fluctuating load demands, and random fault events [10], [11], [12]. A model predictive control-based restoration framework is proposed in [19], where the uncertainties of BS resources in the MG are handled with representative scenarios derived from discrete probability distributions of the forecast errors. Multi-source uncertainties, including the time-varying RES output, load demand, and random fault events, are considered in [20] to restore the DS and improve the system's reliability. In addition, the upstream TG outage duration is also a random event impacting the BS process. Ignoring these uncertainties can lead to suboptimal resource allocation decisions, which may prolong the DS restoration time. Incorporating these uncertainties is critical for robust and effective BS strategies.

Therefore, this paper proposes a frequency-constrained two-stage stochastic resource allocation model within synchronizable dynamic microgrids for black start (SDMG-BS) to address the multi-source uncertainties of BS resource allocation. This model considers the dynamic performance and coordination among restored MGs and with the TG. In summary, the technical contributions of this paper are as follows:

- A dynamic frequency response model for GFMI-based, VSG-embedded BESS with the primary frequency governor (PFG) is developed, introducing constraints on transient frequency indices to enhance MG resilience and frequency security during BS.
- A SDMG-BS framework is proposed to facilitate the restoration of DER-domained DSs. MGs supported by GFMI-based BESS dynamically synchronize at the same frequency through SSWs, accelerating and improving overall recovery.
- A two-stage stochastic resource allocation model in the SDMG-BS is formulated to determine the optimal siting and sizing of GFMI-based BESSs and placement of SSWs, incorporating uncertainties such as RES output, load demand, and TG outage duration to ensure robust and adaptive restoration.

The remainder of this paper is organized as follows. Section II presents the modeling of critical equipment employed in DS restoration. Section III details the formulation of the proposed two-stage stochastic resource allocation model for SDMG-BS. And then, the simulation system and generated uncertainty scenarios are described in Section IV. Further, three cases are designed and studied to validate the developed framework in Section V. Finally, Section VI concludes the whole work.

## II. MODELING OF CRITICAL EQUIPMENT

In this section, the modeling of critical equipment involved in the BS process is presented, with emphasis on the two core BS resources: the GFMI-based BESS and the SSW. First, the sets and notations used throughout the formulation are introduced. Second, the dynamic frequency response of the GFMI-based BESS, which forms the foundation for autonomous restoration, is modeled based on VSG and PFG control principles. Third, the synchronization-enabled SSW, which facilitates the safe interconnection of restored MGs, is modeled to support the dynamic formation of networked MGs. Lastly, the cold load pickup (CLPU) effect is characterized to capture demand surges during restoration.

### A. Preliminary Sets

For a given DS, denoted as $\Gamma = (\mathcal{B}, \mathcal{L}, \Phi)$, where $\mathcal{B}$, $\mathcal{L}$, and $\Phi$ represent the sets of buses, branches, and phases, respectively, the DS is partitioned into multiple segments, referred as bus blocks. These segments, connected via switches, are represented by the set $\mathcal{G}$. Certain segments, identified by the subset $\mathcal{V}$, are

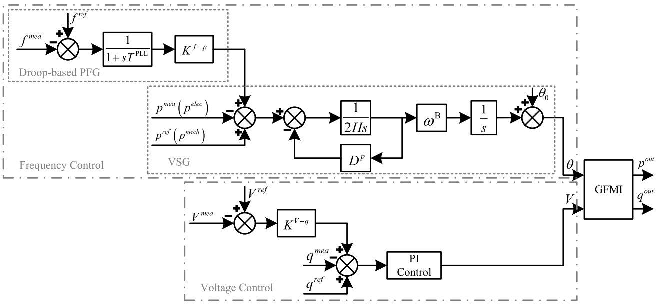

Fig. 1. Control block diagram of the VSG controlled GFMI-based BESS.

selected as candidate locations for BESS installations, facilitating the formation of MGs due to their self-starting capability during BS. A set $\mathcal{W}$ is further defined to ensure that each synchronization occurs only between two distinct MGs, expressed as:

$$\mathcal{W} = \{\{k, l\} | k \in \mathcal{V}, l \in \mathcal{V}, k \neq l\}. \tag{1}$$

The restoration process is modeled over an optimization horizon, represented by the set $\mathcal{T}$, while scenario-based uncertainties are described by the set $\mathcal{O}$.

### *B. Modeling of GFMI-Based BESS*

GFMI-based BESSs act as voltage and frequency reference sources during the restoration process. These systems can self-start and autonomously energize de-energized network segments, form islanded MGs, and support dynamic load pickup.

*1) VSG-Controlled BESS With the PFG:* As shown in Fig. 1, GFMI-based BESSs regulate MG frequency and voltage using frequency and voltage controllers.

With the VSG, at the core of the frequency control loop, a droop-based PFG is employed to further narrow the frequency deviation after load pick-up events [21]. The PFG models the time delay of the phase-locked loop (PLL) while measuring the frequency. Given this structure, for each BESS at $k \in \mathcal{V}$, the transfer function between the variation of the MG frequency $\Delta f_k$ and the change of the electrical load power $\Delta p_k^{elec}$ is expressed as:

$$\Delta f_k = \left[\frac{1 + sT_k^{\text{PLL}}}{s^2 + 2\xi_k \omega_k^n s + (\omega_k^n)^2}\right] \frac{(\omega_k^n)^2 \, \Delta p_k^{elec}}{D_k^p + K_k^{f-p}}, \tag{2a}$$

$$\text{where, } (\omega_k^n)^2 = \frac{D_k^p + K_k^{f-p}}{2H_k T_k^{\text{PLL}}}, \text{ and} \tag{2b}$$

$$\xi_k = \frac{2H_k + D_k^p T_k^{\text{PLL}}}{2\left(D_k^p + K_k^{f-p}\right)} \omega_k^n \tag{2c}$$

Here, $H_k$ and $D_k^p$ are the VSG controller's inertia constant and damping factor, $K_k^{f-p}$ is the droop gain of the droop-based PFG, and $T_k^{\text{PLL}}$ is the time constant of the PLL in the MG $k$. $s$ is a Laplace complex frequency. This represents a second-order frequency response whose natural frequency and damping ratio are $\omega_k^n$ and $\xi_k$, respectively. Note that all the parameters in (2) are defined per unit except for $H_k$ and $T_k^{\text{PLL}}$.

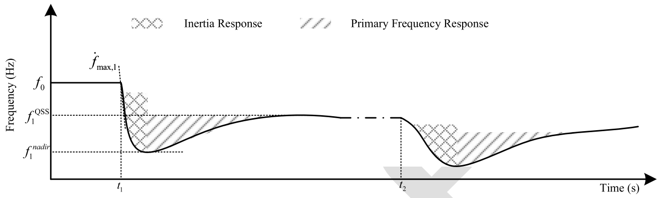

Fig. 2. Typical frequency response curve.

The voltage controller adjusts the terminal voltage to follow the defined V-Q droop ($K^{v-q}$). Since the location of the BESS is an optimization variable, all three-phase buses in MG $k$ are considered as potential sites for installation, represented by the subset $\mathcal{B}_{k,3\phi}$. To comply with the format of the branch power flow of DS, for all $k \in \mathcal{V}$, $n \in \Phi$, and $t \in \mathcal{T}$, the voltage of the GFMI-based BESS at bus $i \in \mathcal{B}_{k,3\phi}$ is controlled as:

$$v_{i,n,t,o} \leq y_i^{\text{BESS}} \left[\left(V_i^b\right)^2 + \Delta v_{i,t,o}^{inc}\right] + (1 - y_i^{\text{BESS}})M, \tag{3a}$$

$$v_{i,n,t,o} \geq y_i^{\text{BESS}} \left[\left(V_i^b\right)^2 + \Delta v_{i,t,o}^{inc}\right] - (1 - y_i^{\text{BESS}})M. \tag{3b}$$

where $v_{i,n,t,o}$ is the square of the voltage magnitude at bus $i$, phase $n$ and time $t$ in scenario $o$, $V_i^b$ is the nominal voltage of bus $i$, $\Delta v_{i,t,o}^{inc}$ is the incremental adjustment of voltage magnitude at bus $i$, $y_i^{\text{BESS}}$ is a binary variable to represent whether the BESS should be installed at bus $i$ or not, and $M$ is a big positive number. Further details about the derivation of the expression of the voltage controller are discussed in Appendix A.

*2) Analytic Expressions of Dynamic Frequency Indices:* As shown in Fig. 2, when there is a load pick-up event, for example, in time $t_1$, the frequency of the GFMI will dynamically respond according to the VSG and PFG's characteristics. Three significant indices can capture this transient process: the RoCoF $f_{\max}^{\text{RoC}}$, the quasi-steady state (QSS) frequency $f^{\text{QSS}}$, and the frequency nadir $f^{nadir}$, separately [22].

During the normal operation period, the frequency of the MG $k \in \mathcal{V}$ is inherited from its QSS frequency at the last time, which implies for all $o \in \mathcal{O}$,

$$f_{k,t,o} = f_{k,t,o}^{\text{QSS}}, \forall t \in \mathcal{T} \setminus (\mathcal{T}^0 \cup \mathcal{T}^{sync}), \tag{4}$$

where $f_{k,t,o}$ is the frequency of the MG $k$, $\mathcal{T}^0$ and $\mathcal{T}^{sync}$ are the sets including the BS beginning time and synchronization moments, individually.

For the established VSG-controlled, GFMI-based BESS with the second-order format in the MG $k$, those dynamic frequency indices at the disturbance moment $t \in \mathcal{T}$ for scenario $o \in \mathcal{O}$ can be expressed as follows,

$$f_{k,t,o,\max}^{\text{RoC}} = \frac{-\Delta p_{k,t,o}^{\text{BESS}}}{2H_k S_{k,nom}^{\text{BESS}}}, \tag{5a}$$

$$f_{k,t,o}^{\text{QSS}} = f_{k,t-1,o} - \frac{\Delta p_{k,t,o}^{\text{BESS}}}{\left(D_k^p + K_k^{f-p}\right) S_{k,nom}^{\text{BESS}}}, \tag{5b}$$

$$f_{k,t,o}^{nadir} = f_{k,t-1,o} - \frac{\Delta p_{k,t,o}^{\text{BESS}} \left(1 + \lambda_k^{nadir}\right)}{\left(D_k^p + K_k^{f-p}\right) S_{k,nom}^{\text{BESS}}}, \tag{5c}$$

$$\lambda_k^{nadir} = \alpha_k^{nadir} \sqrt{1 - \xi_k^2} e^{-\xi_k \omega_k^n t_k^{nadir}}, \tag{5d}$$

$$\alpha_k^{nadir} = \sqrt{\frac{1 - 2T_k^{\text{PLL}} \xi_k \omega_k^n + \left(T_k^{\text{PLL}} \omega_k^n\right)^2}{1 - \xi_k^2}}, \tag{5e}$$

$$t_k^{nadir} = \frac{\arctan\left(\frac{\omega_k^r T_k^{\text{PLL}}}{\xi_k \omega_k^n T_k^{\text{PLL}} - 1}\right)}{\omega_k^r}, \omega_k^r = \omega_k^n \sqrt{1 - \xi_k^2}, \tag{5f}$$

where $\Delta p_{k,t,o}^{\text{BESS}}$ is the total variation of the output of the BESS in MG $k$ at time $t$ versus time $t-1$, which is equal to the $\Delta p_{k,t,o}^{elec}$. $S_{k,nom}^{\text{BESS}}$ is the nominal rated power of the BESS in the MG $k$, $\lambda_k^{nadir}$ is the frequency nadir ratio versus the QSS frequency, $\alpha_k^{nadir}$ is an intermediate parameter for the frequency nadir, $t_k^{nadir}$ is when the frequency reaches to the nadir after the transient process starts. All these three later parameters related to the frequency nadir are constant parameters.

### *C. Modeling of the SSW*

SSWs are deployed to safely interconnect previously energized MGs during the BS process. Each SSW is equipped with embedded synchronism-check logic to verify alignment in voltage magnitude, phase angle, and frequency between the two MGs prior to closure [23]. This capability enables dynamic and controlled formation of networked MGs—an essential step toward coordinated, system-wide restoration.

Before the upstream TG becomes available, GFMI-based BESSs form isolated MGs that autonomously energize nearby segments lacking self-start capability. Dynamically merging these MGs via SSWs not only expands the energized network but also accelerates overall system recovery.

An SSW supports telemetry and remote control and may close only when synchronization conditions are met. These include matched frequency, voltage magnitude, phase sequence, and voltage angle between the two connecting MGs. As shown in [23], when these electrical states are aligned, and branch flow constraints are satisfied, the instantaneous power transfer across the SSW at closure is effectively zero. Therefore, in this work, synchronization criteria are simplified as (i) identical frequency and (ii) zero branch power flow at the switching instant.

To model these capabilities in a tractable and optimization-compatible form, the SSW is represented by three core functions: (i) a frequency monitoring function to assess synchronization readiness; (ii) a frequency coordination function to initiate frequency convergence via GFMI-based BESSs; and (iii) a zero power flow enforcement function to ensure safe, transient-free closure. These functions are detailed in the following content and integrated into the resource allocation framework to support dynamic MG formation.

*1) Frequency Monitoring Function:* This function checks whether the frequency difference between two candidate MGs is within a safe threshold. Synchronization is allowed only when this condition is satisfied.

Given the set storing the location of switches as $\mathcal{L}^{\text{SW}}$, for each $(i,j) \in \mathcal{L}^{\text{SW}}$, a binary variable $u_{ij,t,o}^{\text{SSW}}$ is defined to describe the status of the SSW $(i,j)$, which is dynamically decided during the optimization process as follows:

$$f_{i,t,o} \leq f_{j,t,o} + \left(1 - u_{ij,t,o}^{\text{SSW}}\right) M + \frac{\epsilon}{2}, \tag{6a}$$

$$f_{i,t,o} \geq f_{j,t,o} - \left(1 - u_{ij,t,o}^{\text{SSW}}\right) M - \frac{\epsilon}{2}, \tag{6b}$$

where $f_{i,t,o}$ is the bus $i$'s frequency, $M$ is a big positive number, and $\epsilon$ is the synchronization threshold.

*2) Frequency Coordination Function:* Once synchronization is deemed feasible, this function triggers a signal to the GFMI-based BESS to adjust its frequency, ensuring convergence between the two MGs.

Denote the synchronization signal sent from SSWs to the MG $k$ by $\delta_{k,t,o}^{syn}$, the frequency of the GFMI-based BESS in each MG, which rules other frequencies in other places of the MG it forms, shown in (4), can be modified as follows:

$$f_{k,t,o} = y_k^{\text{BESS}} f_{k,0,o}, \forall t \in \mathcal{T}^0, \tag{7a}$$

$$f_{k,t,o} = f_{k,t,o}^{\text{QSS}} + \delta_{k,t,o}^{syn} \Delta f_{k,t,o}^{syn}, \forall t \in \mathcal{T} \setminus \mathcal{T}^0, \tag{7b}$$

$$\delta_{k,t,o}^{syn} = \textstyle\sum_{(i,j)\in\mathcal{L}^{\text{SW}}} \Delta u_{ij,t,o}^{\text{SSW}} \textstyle\sum_{\{k,l\}\in\mathcal{W}} \Delta u_{kl,t,o}^{syn}, \tag{7c}$$

where $y_k^{\text{BESS}}$ is a binary variable to present whether the BESS is installed at segment $k$ to form an MG to restore the DS, $f_{k,0,o}$ is the value of the frequency of the BESS at the beginning of the BS in scenario $o$, $\Delta f_{k,t,o}^{syn}$ is the synchronization frequency adjustment amount of the MG $k$, and $u_{kl,t,o}^{syn}$ is a binary variable representing the synchronization status between the MG $k$ and $l$.

*3) Zero Power Flow Enforcement Function:* At the switching instant, this function ensures zero active and reactive power flow across the SSW by enforcing matched voltage and phase angle conditions.

For each $(i,j) \in \mathcal{L}^{\text{SW}}$ and $t \in \mathcal{T}$,

$$\boldsymbol{p}_{ij,t,o} \leq \left(1 - \Delta u_{ij,t,o}^{\text{SSW}}\right) \boldsymbol{p}_{ij,\max}, \tag{8a}$$

$$\boldsymbol{p}_{ij,t,o} \geq \left(\Delta u_{ij,t,o}^{\text{SSW}} - 1\right) \boldsymbol{p}_{ij,\max}, \tag{8b}$$

$$\boldsymbol{q}_{ij,t,o} \leq \left(1 - \Delta u_{ij,t,o}^{\text{SSW}}\right) \boldsymbol{q}_{ij,\max}, \tag{8c}$$

$$\boldsymbol{q}_{ij,t,o} \geq \left(\Delta u_{ij,t,o}^{\text{SSW}} - 1\right) \boldsymbol{q}_{ij,\max}, \tag{8d}$$

where $\boldsymbol{p}_{ij,t,o}$ and $\boldsymbol{q}_{ij,t,o}$ are the column vectors storing the branch active and reactive power at switch $ij$, respectively. $\boldsymbol{p}_{ij,\max}$ and $\boldsymbol{q}_{ij,\max}$ are the column vectors storing the maximum active and reactive power for the branch $(i,j)$, respectively.

### *D. Modeling of CLPU*

During BS, initial current demand can surge to several times the nominal level due to simultaneous activation of thermal and motor loads. This phenomenon is known as the CLPU effect [24]. During the CLPU effect, the load current declines exponentially as the loads gradually diversify over time. The duration of this process can vary from minutes to hours.

In addition, the diversified loads in the DS can be classified as the critical load (CL) and the non-critical load (NL) based on their recovery priority. The CLs in a segment must be restored once the power is delivered to this bus block, while the NLs can be restored in an optimal way.

To catch the dynamic process of the CLPU effect and the different recovery properties of the CL and the NL, two staircase-based functions are developed to model the loads. The buses connected with CLs and NLs are collected into $\mathcal{B}^{\text{CL}}$ and $\mathcal{B}^{\text{NL}}$, respectively. For the segment $m \in \mathcal{G}$, the set storing its buses can be noted as $\mathcal{B}_m$. Then, the set including buses in segment $m$ and connected with CLs is defined as $\mathcal{B}^{\text{CL}}_m = \mathcal{B}^{\text{CL}} \cap \mathcal{B}_m$. For each bus $i \in \mathcal{B}^{\text{CL}}_m$, $t \in \mathcal{T}$, and $o \in \mathcal{O}$, the CLs during the BS can be modeled as follows,

$$\boldsymbol{p}^{\text{CL}}_{i,t,o} = \boldsymbol{p}^{\text{DL}}_{i,t,o}\left[\sum\nolimits_{j=1}^{3}\left(\beta_j \Delta u^{\text{SG}}_{m,t-(j-1),o}\right) + u^{\text{SG}}_{m,t,o}\right], \tag{9a}$$

$$\boldsymbol{q}^{\text{CL}}_{i,t,o} = \boldsymbol{p}^{\text{CL}}_{i,t,o} \tan\left(\theta^{\text{CL}}_i\right), \tag{9b}$$

where $\boldsymbol{p}^{\text{CL}}_{i,t,o}$ and $\boldsymbol{p}^{\text{DL}}_{i,t,o}$ are column vectors storing the restored and nominal active load demand at bus $i$, time $t$, and scenario $o$, separately. $\beta_1$, $\beta_2$, and $\beta_3$ are the CLPU coefficients. $u^{\text{SG}}_{m,t,o}$ is a binary variable representing the energized status of the segment $m$, which highlights the priority of the CL in a segment. $\boldsymbol{q}^{\text{CL}}_{i,t,o}$ and $\boldsymbol{q}^{\text{DL}}_{i,t,o}$ are column vectors storing the restored reactive CL demand and actual reactive load demand at bus $i$, time $t$, and scenario $o$, individually. $\theta^{\text{CL}}_i$ is the power factor angle of the CL at bus $i$.

Similarly, the set including buses in segment $m$ and connected with NLs is defined as $\mathcal{B}^{\text{NL}}_m = \mathcal{B}^{\text{NL}} \cap \mathcal{B}_m$. For each bus $i \in \mathcal{B}^{\text{NL}}_m$, $t \in \mathcal{T}$, and $o \in \mathcal{O}$, the NLs is modeled as,

$$\boldsymbol{p}^{\text{NL}}_{i,t,o} = \boldsymbol{p}^{\text{DL}}_{i,t,o}\left[\sum\nolimits_{j=1}^{3}\left(\beta_j \Delta z^{\text{B}}_{i,t-(j-1),o}\right) + z^{\text{B}}_{i,t,o}\right], \tag{10a}$$

$$\boldsymbol{q}^{\text{NL}}_{i,t,o} = \boldsymbol{p}^{\text{NL}}_{i,t,o} \tan\left(\theta^{\text{NL}}_i\right), \tag{10b}$$

$$z^{\text{B}}_{i,t,o} \leq u^{\text{SG}}_{m,t,o}, z^{\text{B}}_{i,t-1,o} \leq z^{\text{B}}_{i,t,o}, \tag{10c}$$

where $\boldsymbol{p}^{\text{NL}}_{i,t,o}$ and $\boldsymbol{q}^{\text{NL}}_{i,t,o}$ are column vectors storing the restored active and reactive NL demand at bus $i$, time $t$, and scenario $o$, separately. $z^{\text{B}}_{i,t,o}$ is a binary variable representing the energized status of the NL at bus $i$, time $t$, and scenario $o$, which is dominated by the segment status. $\theta^{\text{NL}}_i$ is the power factor angle of the NL at bus $i$.

## III. MATHEMATICAL FORMULATION

In this section, we first describe the resource allocation process for deploying BS resources at the initial stage. Next, we formulate the SDMG-BS framework for the DS at the second stage. Finally, we present a comprehensive narration of this two-stage stochastic model.

### A. First Stage Resource Allocation Problem

*1) Objective of Resource Allocation:* The objective of the resource allocation stage is to minimize the total investment cost associated with the deployment of BS resources. Noting that the minimum number of SSWs required to enable dynamic MG formation equals the number of deployed GFMI-based BESS units minus one, the first-stage allocation problem can be formulated as the following optimization:

$$\min F^{alloc} = \sum\nolimits_{k \in \mathcal{V}}\left(y^{\text{BESS}}_k + S^{\text{BESS}}_{k,nom} + E^{\text{BESS}}_{k,nom}\right), \tag{11}$$

where $F^{alloc}$ is the allocation objective, and $E^{\text{BESS}}_{k,nom}$ denotes the nominal rated capacity of the BESS for MG $k \in \mathcal{V}$.

*2) Constraints on BESS Allocation Inside MGs:* For each MG $k \in \mathcal{V}$, the installed GFMI-based BESS at its three-phase buses, satisfying,

$$y^{\text{BESS}}_i S^{\text{BESS}}_{\min} \leq S^{\text{BESS}}_{i,nom} \leq y^{\text{BESS}}_i S^{\text{BESS}}_{\max}, \tag{12a}$$

$$y^{\text{BESS}}_i E^{\text{BESS}}_{\min} \leq E^{\text{BESS}}_{i,nom} \leq y^{\text{BESS}}_i E^{\text{BESS}}_{\max}, \tag{12b}$$

where $S^{\text{BESS}}_{\min}$, $S^{\text{BESS}}_{\max}$ are the minimum and maximum allowable rated powers, and $E^{\text{BESS}}_{\min}$, $E^{\text{BESS}}_{\max}$ are the minimum and maximum allowable capacities for a single BESS. The nominal capacity $E^{\text{BESS}}_{i,nom}$ pertains to the BESS at bus $i \in \mathcal{B}_{k,3\phi}$.

Additionally, each MG requires exactly one GFMI-based BESS to provide frequency and voltage references before merging with other MGs:

$$\sum\nolimits_{i \in \mathcal{B}_{k,3\phi}} y^{\text{BESS}}_i = y^{\text{BESS}}_k, \tag{13a}$$

$$\sum\nolimits_{i \in \mathcal{B}_{k,3\phi}} S^{\text{BESS}}_{i,nom} = S^{\text{BESS}}_{k,nom}, \tag{13b}$$

$$\sum\nolimits_{i \in \mathcal{B}_{k,3\phi}} E^{\text{BESS}}_{i,nom} = E^{\text{BESS}}_{k,nom}, \tag{13c}$$

while the (13c) is stated to simplify the expression of the formulation.

*3) Constraints on BESS Allocation Among MGs:* To ensure the BS process is successful, at least one MG should be available before the TG is available. In addition, the total deployed BESS resources for the BS are restricted by the DS budget. These requirements among the MGs can be concluded as,

$$\sum\nolimits_{k \in \mathcal{V}} y^{\text{BESS}}_k \geq 1, \tag{14a}$$

$$\sum\nolimits_{k \in \mathcal{V}} S^{\text{BESS}}_{k,nom} \leq S^{\text{BESS}}_{budget}, \tag{14b}$$

$$\sum\nolimits_{k \in \mathcal{V}} E^{\text{BESS}}_{k,nom} \leq E^{\text{BESS}}_{budget}, \tag{14c}$$

where $S^{\text{BESS}}_{budget}$ and $E^{\text{BESS}}_{budget}$ are the overall budgets for the rated power and capacity of the BESS assigned to the BS, respectively.

*4) Constraints on SSW Allocation:* Some ESWs are replaced with SSWs to enable synchronization during BS. To minimize costs and maximize flexibility, the number of deployed SSWs is constrained as,

$$\sum\nolimits_{(i,j) \in \mathcal{L}^{\text{SW}}} y^{\text{SSW}}_{ij} = \sum\nolimits_{k \in \mathcal{V}} y^{\text{BESS}}_k - 1, \tag{15}$$

where $y^{\text{SSW}}_{ij}$ is a binary variable to present whether the switch at $(i,j)$ is replaced with a SSW.

### B. Second Stage SDMG-BS Problem

*1) Objective of BS:* The second-stage objective is to maximize the total restored loads over the restoration horizon,

$$\begin{aligned}\max F^{restor}_o = \sum\nolimits_{t \in \mathcal{T}}\Big[&\gamma^{\text{CL}} \sum\nolimits_{i \in \mathcal{B}^{\text{CL}}}\left(\mathbf{1}^T_{|\Phi_i|}\boldsymbol{p}^{\text{CL}}_{i,t,o}\right)\\ &+\gamma^{\text{NL}} \sum\nolimits_{i \in \mathcal{B}^{\text{NL}}}\left(\mathbf{1}^T_{|\Phi_i|}\boldsymbol{p}^{\text{NL}}_{i,t,o}\right)\Big]\Delta t,\end{aligned} \tag{16}$$

where $F_o^{restor}$ is the objective function of the BS in scenario $o$, $\gamma^{\mathrm{CL}}$ and $\gamma^{\mathrm{NL}}$ are weighting coefficients for the CL and NL, separately. $\Phi_i$ is the set storing the phases of loads connected at bus $i$, $\mathbf{1}^T_{|\Phi_i|}$ is the transpose of a column vector with all $|\Phi_i|$ elements being one, $\Delta t$ is the duration between $t$ and $t-1$.

*2) Constraints on BS Energization:*

*a) Energizing switches (ESW) action:* For each switch $(i,j) \in \mathcal{L}^{\mathrm{SW}}$, if it's not chosen to be replaced with the SSW, it operates as an ESW during the BS, whose action is constrained as,

$$u^{\mathrm{ESW}}_{ij,t,o} \le 1 - y^{\mathrm{SSW}}_{ij}, \tag{17a}$$

$$u^{\mathrm{ESW}}_{ij,t,o} \le u^{\mathrm{B}}_{i,t-1,o} + u^{\mathrm{B}}_{j,t-1,o}, \tag{17b}$$

$$\Delta u^{\mathrm{ESW}}_{ij,t,o} \le 2 - u^{\mathrm{B}}_{i,t-1,o} - u^{\mathrm{B}}_{j,t-1,o}, \tag{17c}$$

where $u^{\mathrm{ESW}}_{ij,t,o}$ is a binary variable to indicate whether the ESW $(i,j)$ is closed, $u^{\mathrm{B}}_{i,t,o}$ is a binary variable to present the energized status of the bus $i$ of the ESW $(i,j)$. As shown in (17a), the action of the ESW $(i,j)$ will be blocked if the SSW is placed here. The ESW $(i,j)$ can act to energize other non-MG segments once one end of it belongs to a powered MG, but it cannot be used to synchronize two operated MGs as depicted in (17b) and (17c).

*b) SSWs action:* If a switch $(i,j) \in \mathcal{L}^{\mathrm{SW}}$ is chosen to be replaced with a SSW, it will be capable of synchronizing two MGs during the BS, whose action is constrained as,

$$u^{\mathrm{SSW}}_{ij,t,o} \le y^{\mathrm{SSW}}_{ij}, \tag{18a}$$

$$u^{\mathrm{SSW}}_{ij,t,o} \ge u^{\mathrm{SSW}}_{ij,t-1,o}, \tag{18b}$$

$$2u^{\mathrm{SSW}}_{ij,t,o} \le u^{\mathrm{B}}_{i,t-1,o} + u^{\mathrm{B}}_{j,t-1,o}, \tag{18c}$$

where $u^{\mathrm{SSW}}_{ij,t,o}$ is a binary variable to indicate whether the SSW $(i,j)$ is closed, and $\epsilon$ is a small positive number. As illustrated in (18a), the SSW $(i,j)$ will be blocked if it is not deployed. Eq (18b) shows that the action of SSW is irreversible. Eq (18c) requires the SSW $(i,j)$ can only be used to do the synchronization.

*c) Segment energization status:* Given the set storing the non-switchable line of DS as $\mathcal{L}^{\mathrm{LN}}$, and the set collecting the branch inside a segment $m \in \mathcal{G}$ as $\mathcal{L}_m$, the set including the lines inside the segment $m$ can be defined as $\mathcal{L}^{\mathrm{LN}}_m = \mathcal{L}^{\mathrm{LN}} \cap \mathcal{L}_m$. Similarly, the set holding the switch inside a segment can be defined as $\mathcal{L}^{\mathrm{SW}}_m = \mathcal{L}^{\mathrm{SW}} \cap \mathcal{L}_m$. And then, for each segment $m$, its energization status is constrained as follows,

$$u^{\mathrm{SG}}_{m,t,o} \ge u^{\mathrm{SG}}_{m,t-1,o}, \tag{19a}$$

$$u^{\mathrm{SG}}_{m,t,o} = u^{\mathrm{B}}_{i,t,o}, \forall i \in \mathcal{B}_m, \tag{19b}$$

$$u^{\mathrm{SG}}_{m,t,o} = u^{\mathrm{L}}_{ij,t,o}, \forall (i,j) \in \mathcal{L}^{\mathrm{LN}}_m, \tag{19c}$$

$$u^{\mathrm{SG}}_{m,t,o} \ge u^{\mathrm{ESW}}_{ij,t,o}, \forall (i,j) \in \mathcal{L}^{\mathrm{SW}}_m, \tag{19d}$$

$$\textstyle\sum_{(i,j)\in\mathcal{L}^{\mathrm{SW}}_m} \Delta u^{\mathrm{ESW}}_{ij,t,o} \le u^{\mathrm{SG}}_{m,t-1,o} M + 1, \tag{19e}$$

where $u^{\mathrm{L}}_{ij,t,o}$ is a binary variable that stands for the energized status of the branch $(i,j)$. As described in (19a), once the segment is energized, it will be powered until the end of the optimization. Meanwhile, all the buses and non-switchable lines inside the segment should have the same status as the segment itself, as shown in (19b) and (19c). The black-out segment can only be energized by one of ESWs belonging to it at the same time, as shown in (19d) and (19e).

*d) Radiality of the DS:* The radial topology of DS is required to maintain during the BS, which is dynamically constrained as follows,

$$\sum_{(i,j)\in\mathcal{L}} u^{\mathrm{L}}_{ij,t,o} = \sum_{i\in\mathcal{B}} u^{\mathrm{B}}_{i,t,o} - R_{t,o}, \tag{20a}$$

$$R_{t,o} = \sum_{k\in\mathcal{V}} y^{\mathrm{BESS}}_k + \sum_{i\in\mathcal{B}^{\mathrm{TG}}} u^{\mathrm{B}}_{i,t,o} - \sum_{(i,j)\in\mathcal{L}^{\mathrm{SW}}} u^{\mathrm{SSW}}_{ij,t,o}, \tag{20b}$$

where $R_{t,o}$ is the number of root buses, $\mathcal{B}^{\mathrm{TG}}$ is the set collecting the TG buses. The radiality of DS is guaranteed by (20a), while $R_{t,o}$ is dynamically decided during the BS process in (20b).

*3) Constraints on Synchronization Processes:*

*a) Frequency consensus constraints:* Define the set, including buses at of switches belonging to segment $k$, as $\mathcal{B}^{\mathrm{SW}}_k$. Then, for each $k \in \mathcal{V}$, the frequencies of bus $i \in \mathcal{B}^{\mathrm{SW}}_k$ inside the MG $k$ are ruled as follows,

$$f_{i,t,o} \le f_{k,t,o} + (1 - y^{\mathrm{BESS}}_k) M, \tag{21a}$$

$$f_{i,t,o} \ge f_{k,t,o} - (1 - y^{\mathrm{BESS}}_k) M. \tag{21b}$$

Furthermore, for each general segment $m \in \mathcal{G}$, the frequencies of bus $i \in \mathcal{B}^{\mathrm{SW}}_m$ should be uniform at every moment due to their same energized status shown in (19b), which is concluded as follows,

$$f_{i,t,o} = f_{j,t,o}, \forall j \in \mathcal{B}^{\mathrm{SW}}_m, j \ne i. \tag{22}$$

*b) Frequency propagation constraints:* Once a ESW $(i,j) \in \mathcal{L}^{\mathrm{SW}}$ is closed to pick up a non-MG segment, the frequency of the MG it is associated with is passed to that new energized segment as follows,

$$f_{i,t,o} \le f_{j,t,o} + \left(1 - u^{\mathrm{ESW}}_{ij,t,o}\right) M, \tag{23a}$$

$$f_{i,t,o} \ge f_{j,t,o} - \left(1 - u^{\mathrm{ESW}}_{ij,t,o}\right) M, \tag{23b}$$

*c) Synchronization indicative constraints:* Based on the propagation mechanism of frequency during the energization stage of BS depicted in Eqs. (21) to (23), the synchronization moment happening between the MG $k$ and $l$ in the set $\mathcal{V}$ at time $t \in \mathcal{T}$ in scenario $o \in \mathcal{O}$, where $\{k,l\} \in \mathcal{W}$, can be captured as,

$$u^{syn}_{kl,t,o} \ge u^{syn}_{kl,t-1,o}, \tag{24a}$$

$$(2 - y^{\mathrm{BESS}}_k - y^{\mathrm{BESS}}_l) = \mu_{kl}, \tag{24b}$$

$$u^{syn_-}_{kl,t,o} + u^{syn}_{kl,t,o} + u^{syn_+}_{kl,t,o} = 1, \tag{24c}$$

$$\epsilon u^{syn_-}_{kl,t,o} - \frac{\epsilon}{2} u^{syn}_{kl,t,o} - M u^{syn_+}_{kl,t,o} \le f_{l,t,o} - f_{k,t,o} + \mu_{kl}, \tag{24d}$$

$$M u^{syn_-}_{kl,t,o} + \frac{\epsilon}{2} u^{syn}_{kl,t,o} - \epsilon u^{syn_+}_{kl,t,o} \ge f_{l,t,o} - f_{k,t,o} + \mu_{kl}, \tag{24e}$$

where $\mu_{kl}$ is an intermediate variable standing for whether deploying GFMI-based BESS inside the segment $k$ and $l$ at the same time. $u^{syn_-}_{kl,t,o}$ and $u^{syn_+}_{kl,t,o}$ are the binary variables representing the left and right synchronization indicators between the MG $k$ and $l$, respectively.

Additionally, to decrease the inrush current of the GFMI-based BESS at the synchronization moment, the number of MGs merged into another MG should be restricted to one. For any two elements $\{k, l\}$ and $\{m, n\}$ in $\mathcal{W}$, define the set $\mathcal{X} = \{\{k, l, m, n\}\}$, where $|\{k, l\} \cap \{m, n\}| = 1$. And then, for each $\{k, l, m, n\} \in \mathcal{X}$, the above extra synchronization constraint is modeled as,

$$\Delta u^{syn}_{kl,t,o} + \Delta u^{syn}_{mn,t,o} - u^{syn}_{ln,t,o} \le 1, \tag{25}$$

where $\{l, n\} = (\{k, l\} \cup \{m, n\}) \setminus (\{k, l\} \cap \{m, n\})$.

4) *Constraints on System Operation:*

*a) TG outage and recovery:* The TG is unavailable during the BS until the fault transmission line is repaired. Given the set storing the TG bus as $\mathcal{B}^{\text{TG}}$, the output and status of TG $i \in \mathcal{B}^{\text{TG}}$ is constrained with its indicative binary variable $u^{\text{TG}}_{i,t,o}$ at each $t \in \mathcal{T}$ and $o \in \mathcal{O}$ as follows,

$$\boldsymbol{v}_{i,t,o} = u^{\text{TG}}_{i,t,o} \mathbf{1}_{|\Phi|}, \tag{26a}$$

$$f^{\text{TG}}_{i,t,o} = 60 u^{\text{TG}}_{i,t,o}, \tag{26b}$$

$$\left(\tfrac{1}{3} S^{\text{TG}}_{i,max}\right)^2 \ge \max_{n\in\Phi} \left\{ \left(p^{\text{TG}}_{i,n,t,o}\right)^2 + \left(q^{\text{TG}}_{i,n,t,o}\right)^2 \right) \right\}, \tag{26c}$$

where $p^{\text{TG}}_{i,n,t,o}$ and $q^{\text{TG}}_{i,n,t,o}$ are the active and reactive output of TG's nth phase. $S^{\text{TG}}_{i,max}$ is the maximum rated power of TG at bus $i$. $f^{\text{TG}}_{i,t,o}$ is the TG's frequency.

*b) Model of BESS:* The output of the BESS at bus $i \in \mathcal{B}_{k,3\phi}$ for each $k \in \mathcal{V}$ is constrained by the planned rated power and capacity at the first stage, which is illustrated as follows,

$$SoC_{i,t,o} = SoC_{i,t-1,o} - \mathbf{1}^T_{|\Phi_i|} \boldsymbol{p}^{\text{BESS}}_{i,t,o} / E^{\text{BESS}}_{i,nom}, \tag{27a}$$

$$\lfloor SoC \rfloor \le SoC_{i,t,o} \le \lceil SoC \rceil, \tag{27b}$$

$$\left(\tfrac{1}{3} S^{\text{BESS}}_{i,nom}\right)^2 \ge \max_{n\in\Phi} \left\{ \left(p^{\text{BESS}}_{i,n,t,o}\right)^2 + \left(q^{\text{BESS}}_{i,n,t,o}\right)^2 \right) \right\}, \tag{27c}$$

where $\boldsymbol{p}^{\text{BESS}}_{i,t,o}$ and $\boldsymbol{q}^{\text{BESS}}_{i,t,o}$ are the column vectors collecting the active and reactive output of the BESS at bus $i$, separately. $p^{\text{BESS}}_{i,n,t,o}$ and $q^{\text{BESS}}_{i,n,t,o}$ are the $n$-th phase value of $\boldsymbol{p}^{\text{BESS}}_{i,t,o}$ and $\boldsymbol{q}^{\text{BESS}}_{i,t,o}$, separately. $SoC_{i,t,o}$ is the state of charge (SoC) of the BESS at bus $i$.

In addition, the next constraints are introduced to express the active output of the BESS belonging to the MG $k \in \mathcal{V}$,

$$\boldsymbol{p}^{\text{BESS}}_{k,t,o} = \textstyle\sum_{i\in\mathcal{B}_{k,3\phi}} \boldsymbol{p}^{\text{BESS}}_{i,t,o}. \tag{28}$$

*c) Frequency security constraints:* Given the dynamic frequency indices of the transient process and the full frequency expression under normal operation in (5) and (7), respectively, for each $k \in \mathcal{V}$ and $t \in \mathcal{T}$, the following constraints are introduced to guarantee the frequency security during the transient and normal process of the BS,

$$\lfloor f^{\text{RoC}}_{\max} \rfloor \le f^{\text{RoC}}_{k,t,o,\max} \le \lceil f^{\text{RoC}}_{\max} \rceil, \tag{29a}$$

$$\lfloor f^{\text{QSS}} \rfloor \le f^{\text{QSS}}_{k,t,o} \le \lceil f^{\text{QSS}} \rceil, \tag{29b}$$

$$\lfloor f^{nadir} \rfloor \le f^{nadir}_{k,t,o} \le \lceil f^{nadir} \rceil, \tag{29c}$$

$$\lfloor f_k \rfloor \le f_{k,t,o} \le \lceil f_k \rceil, \tag{29d}$$

where $\lfloor \cdot \rfloor$ and $\lceil \cdot \rceil$ are the lower and upper limit operators of a variable, respectively.

*d) Model of PV:* The active power output of a behind-the-meter PV system depends on the fluctuating environmental conditions, such as solar irradiance and temperature. Meanwhile, its reactive power output is controlled to maintain a fixed power factor, as specified by the grid operator. According to IEEE Std 1547-2018 [25], DERs, including PV systems, are permitted to operate in constant power factor mode, where reactive power is proportionally adjusted to match a specified ratio with active power output.

Given the set containing the buses with PV systems as $\mathcal{B}^{\text{PV}}$, for each bus $i \in \mathcal{B}^{\text{PV}}$, let $\eta_{i,t,o}$ denote its real-time output ratio, the active and reactive power injections are expressed in vector form as follows.

$$\boldsymbol{p}^{\text{PV}}_{i,t,o} = \tfrac{1}{3} S^{\text{PV}}_{i,nom} \eta_{t,o} \mathbf{1}_{|\Phi_i|}, \tag{30a}$$

$$\boldsymbol{q}^{\text{PV}}_{i,t,o} = 0.352 \boldsymbol{p}^{\text{PV}}_{i,t,o}, \tag{30b}$$

where $\boldsymbol{p}^{\text{PV}}_{i,t,o}$ and $\boldsymbol{q}^{\text{PV}}_{i,t,o}$ are the column vectors collecting the active and reactive output of the PV at bus $i$, respectively. $S^{\text{PV}}_{i,nom}$ is the nominal rated power of the PV at bus $i$. $|\cdot|$ is an operator calculating the cardinality of a set.

This formulation ensures that the inverter adheres to the fixed power factor requirement while responding to time-varying solar generation. A detailed derivation of this modeling approach is provided in [26].

*e) Unbalanced linear power flow:* Define the set collecting the child buses of bus $i$ as $\mathcal{B}^{ch}_i$, the nodal power balance constraints for all $i \in \mathcal{B}$ at time $t \in \mathcal{T}$ in scenario $o \in \mathcal{O}$ can be expressed as follow,

$$\boldsymbol{p}_{i,t,o} = \sum_{j\in\mathcal{B}^{ch}_i} \left( \boldsymbol{\Lambda}_{|\Phi_{hi}|\times|\Phi_{ij}|} \boldsymbol{p}_{ij,t,o} \right) - \boldsymbol{p}_{hi,t,o} \tag{31a}$$

$$\boldsymbol{q}_{i,t,o} = \sum_{j\in\mathcal{B}^{ch}_i} \left( \boldsymbol{\Lambda}_{|\Phi_{hi}|\times|\Phi_{ij}|} \boldsymbol{q}_{ij,t,o} \right) - \boldsymbol{q}_{hi,t,o}, \tag{31b}$$

$$\boldsymbol{p}_{i,t,o} = \boldsymbol{p}^{\text{TG}}_{i,t,o} + \boldsymbol{p}^{\text{BESS}}_{i,t,o} + \boldsymbol{p}^{\text{PV}}_{i,t,o} - \boldsymbol{p}^{\text{CL}}_{i,t,o} - \boldsymbol{p}^{\text{NL}}_{i,t,o} \tag{31c}$$

$$\boldsymbol{q}_{i,t,o} = \boldsymbol{q}^{\text{TG}}_{i,t,o} + \boldsymbol{q}^{\text{BESS}}_{i,t,o} + \boldsymbol{q}^{\text{PV}}_{i,t,o} - \boldsymbol{q}^{\text{CL}}_{i,t,o} - \boldsymbol{q}^{\text{NL}}_{i,t,o} \tag{31d}$$

where $\boldsymbol{p}_{i,t,o}$ and $\boldsymbol{q}_{i,t,o}$ are the column vectors storing the injection active and reactive power at bus $i$, individually. $\Phi_{ij}$ is a set including the phases of branch $ij$. $\boldsymbol{\Lambda}_{|\Phi_{hi}|\times|\Phi_{ih}|}$ is a matrix with $|\Phi_{hi}|$ rows and $|\Phi_{ij}|$ columns, whose elements in $\Phi_j$ row all are one.

The phase voltages located at the ends of a branch $(i, j) \in \mathcal{L}$ at time $t \in \mathcal{T}$ in scenario $o \in \mathcal{O}$ are combined with the following constraints,

$$\begin{aligned}\boldsymbol{v}_{j,t,o} \le\ & \Big[\boldsymbol{v}^{\Phi_{ij}}_{i,t,o} - 2\left(\boldsymbol{r}_{ij}\boldsymbol{p}_{ij,t,o} + \boldsymbol{x}_{ij}\boldsymbol{q}_{ij,t,o}\right) \\ & + \left(1 - u^{\text{L}}_{ij,t,o}\right)\boldsymbol{M}^{\Phi_{ij}}\Big],\end{aligned} \tag{32a}$$

$$\begin{aligned}\boldsymbol{v}_{j,t,o} \ge\ & \Big[\boldsymbol{v}^{\Phi_{ij}}_{i,t,o} - 2\left(\boldsymbol{r}_{ij}\boldsymbol{p}_{ij,t,o} + \boldsymbol{x}_{ij}\boldsymbol{q}_{ij,t,o}\right) \\ & - \left(1 - u^{\text{L}}_{ij,t,o}\right)\boldsymbol{M}^{\Phi_{ij}}\Big],\end{aligned} \tag{32b}$$

with,

$$u^{\rm L}_{ij,t} = u^{\rm ESW}_{ij,t} + u^{\rm SSW}_{ij,t}, \forall (i,j) \in \mathcal{L}^{\rm SW}, \tag{33}$$

where $\boldsymbol{v}_{j,t,o}$ is a column vector storing the square of the voltage magnitude at bus $j$, $\cdot^{\Phi_{ij}}$ is an operator extracting the phase elements of branch $(i,j)$. $\boldsymbol{r}_{ij}$ and $\boldsymbol{x}_{ij}$ are matrices associated with branch resistance and reactance, whose calculations are described in [27].

Moreover, to keep the normal operation of the restored segments, for each $(i,j) \in \mathcal{L}$ and $i \in \mathcal{B}$, the following constraints need to be satisfied,

$$-u^{\rm L}_{ij,t,o}\boldsymbol{p}_{ij,\max} \leq \boldsymbol{p}_{ij,t,o} \leq u^{\rm L}_{ij,t,o}\boldsymbol{p}_{ij,\max}, \tag{34a}$$

$$-u^{\rm L}_{ij,t,o}\boldsymbol{q}_{ij,\max} \leq \boldsymbol{q}_{ij,t,o} \leq u^{\rm L}_{ij,t,o}\boldsymbol{q}_{ij,\max}, \tag{34b}$$

$$u^{\rm B}_{i,t,o}\lfloor \boldsymbol{v}_i \rfloor \leq \boldsymbol{v}_{i,t,o} \leq u^{\rm B}_{i,t,o}\lceil \boldsymbol{v}_i \rceil, \tag{34c}$$

where $\boldsymbol{p}_{ij,\max}$ and $\boldsymbol{q}_{ij,\max}$ are the column vectors storing the maximum active and reactive power for the branch $(i,j)$, respectively.

### C. Full Resource Allocation Formulation in SDMG-BS

The complete two-stage stochastic resource allocation model integrates the objectives and constraints from the first and second stages as follows,

$$\min \quad F^{alloc} - \zeta \sum_{o \in \mathcal{O}} \pi_o F^{restor}_o, \tag{35}$$

$$\text{s.t.} \quad \text{Resoure Allocation Constraints: Eq. } (12) \sim (15), \tag{36}$$

$$\text{Switches Action Constraints: Eq. } (17) \sim (18), \tag{37}$$

$$\text{Energization Constraints: Eq. } (19) \sim (20), \tag{38}$$

$$\text{Synchronization Constraints: Eq. } (8), (21) \sim (25), \tag{39}$$

$$\text{Frequency Security Constraints: Eq. } (5), (7), (29), \tag{40}$$

$$\text{Power Flow Constraints: Eq. } (3), (31) \sim (34), \tag{41}$$

$$\text{CLPU Constraints: Eq. } (9) \sim (10), \tag{42}$$

$$\text{Power source Output Constraints: Eq. } (27) \sim (30), \tag{43}$$

where $\zeta$ is the scaling weight in \$/kWh and $\pi_o$ is the probability of the scenario $o$.

*Scalability Remark:* As a long-term planning model, the proposed SDMG-BS formulation emphasizes optimality and robustness over real-time computation speed. While additional binary variables are introduced—particularly to handle flexible synchronization among dynamically formed MGs—these variables grow with the number of candidate BESS locations. Specifically, the synchronization indicative constraints, shown in Eqs. (24) and (25)), scale as $(3T+1)\binom{n}{2}$ for $n$ BESS candidates and $T$ time steps. In practice, however, geographical and electrical constraints often limit BESS deployment to a small subset of three-phase buses, thereby ensuring the model remains computationally tractable for realistic system sizes.

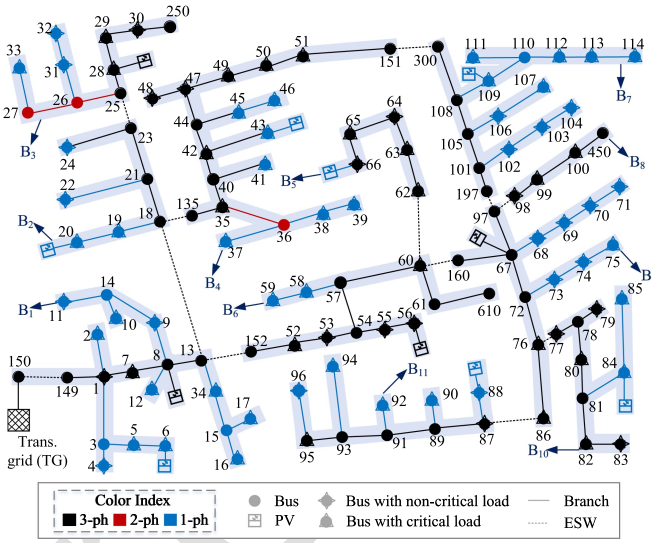

Fig. 3. Modified IEEE 123-node feeder diagram.

## IV. Simulation Setup

In this section, we first outline the adopted simulation system and parameters. Following this, we explain the defined uncertainty scenarios.

### A. System Architecture and Parameters

The three-phase unbalanced IEEE 123-node feeder is employed to design the BS plan for the DS. The modified DS diagram is shown in Fig. 3. The system comprises 88 buses connected to loads, of which 52 are critical loads. The maximum active load demand of the entire system is approximately 3.49 MW, while all loads within the system are assumed to share a uniform power factor $\theta = 0.484$ . Behind-the-meter PV systems, with a total installed capacity of 965kW, account for 28% of the system's active load demand.

As depicted in Fig. 3, the test system is divided into 12 sections, including 11 segments ($\mathrm{B}_i, i \in \mathcal{G}$) and the TG, separated by 12 ESW, represented by the dashed line. During the resource allocation stage, a three-phase bus within selected segments is chosen as the site for installing GFMI-based BESSs. The maximum allowable rated power and capacity for the BESSs, constrained by the DS budget, are 6.5 MW and 10MWh, respectively, which also represent the maximum limits for a single BESS. Conversely, the minimum rated power and capacity for a single BESS, limited by technology constraints, are 0.1 MW and 1MWh, respectively.

Key parameters for the VSG controller of the BESS are as follows: inertia constant $H = 8$ s, PLL time constant $T^{\rm PLL} = 0.05$ s, damping factor $D^p = 1$ (per unit), and droop gain $K^{f-p} = 89$ (per unit). The safe operation ranges for the frequency, QSS frequency, frequency nadir, and maximum RoCoF, are $(59.50 \sim 60.50)$ Hz, $(59.50 \sim 60.50)$ Hz, $(57.80 \sim 61.80)$ Hz, and $(-4.00 \sim 4.00)$ Hz/s, individually.

### B. Generated Scenarios

Uncertainties considered during the BS process include PV system output, load demand, and TG outage duration. The PV

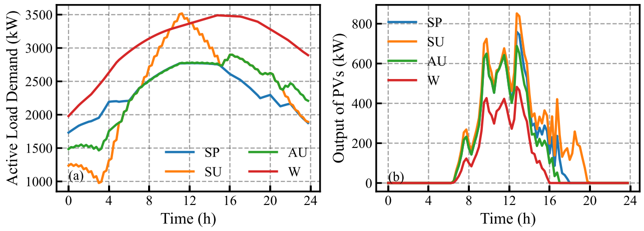

Fig. 4. Season-based load and PV curves. (a) Active load demand. (b) PV output. (SP: Spring, SU: Summer, AU: Autumn, W: Winter).

TABLE I
OUTAGE DURATION PROBABILITY

| Duration (min) | 60 | 120 | 180 | 240 |
|---|---|---|---|---|
| Probability | 0.1340 | 0.4290 | 0.2733 | 0.1637 |

output and load demand uncertainties follow Beta and Normal distributions, respectively. Season-based characteristic curves for PV output and load demand are derived using sampling and clustering techniques, as illustrated in Fig. 4.

The TG outage duration uncertainty is modeled using discrete probabilities obtained from historical data, as shown in Table. I.

Assuming equal probabilities for season-based characteristic curves, the combined probabilities of the 16 scenarios, defined by season $\sigma \in \{\mathrm{SP}, \mathrm{SU}, \mathrm{AU}, \mathrm{W}\}$ and TG outage duration $\nu \in \{60, 120, 180, 240\}$, are given by:

$$\pi_o = \pi_\sigma \pi_\nu = 0.25\pi_\nu, \forall o = \{\sigma, \nu\}. \tag{44}$$

## V. RESULTS

In this section, firstly, the stochastic plan is presented and compared with deterministic plans in Case 1. Secondly, the detailed BS process of the stochastic plan under the extreme scenario is illustrated in Case 2. Finally, the frequency security across all scenarios is analyzed in Case 3.

### A. Case 1: Verification of Dynamic Frequency Responses

The modified DS shown in Fig. 3, which incorporates the GFMI-based BESS model introduced in Section II, is implemented in DIgSILENT PowerFactory to conduct root-mean-square (RMS) simulations for validating dynamic frequency responses during the BS process.

To evaluate the accuracy of the proposed analytical expressions for key dynamic frequency indices, including $f_{\max}^{\mathrm{ROC}}$, $f^{nadir}$, and $f^{\mathrm{QSS}}$ defined in (5), load pick-up events of various magnitudes are triggered at randomly selected locations within the islanded MG. The simulation results are compared against the estimated values derived from the proposed expressions. Table II summarizes the comparison results, and the average estimation accuracy $\tau$ is computed for each index.

As shown in Table II, all three frequency indices exhibit high estimation accuracy, exceeding 90% in all cases, which supports the validity of the proposed analytical expressions.

TABLE II
VALIDATION OF ESTIMATED FREQUENCY INDICES

| $\Delta p^{\mathrm{L}}$ (MW) | $f_{\max}^{\mathrm{ROC}}$ (Hz/s) |  | $f^{\mathrm{nadir}}$ (Hz) |  | $f^{\mathrm{QSS}}$ (Hz) |  |
|---|---|---|---|---|---|---|
|  | Meas. | Est. | Meas. | Est. | Meas. | Est. |
| 1 | -0.353 | -0.378 | 59.963 | 59.964 | 59.966 | 59.967 |
| 2 | -0.706 | -0.750 | 59.925 | 59.927 | 59.932 | 59.933 |
| 10 | -3.611 | -3.750 | 59.616 | 59.636 | 59.649 | 59.667 |
| $\tau(\%)$ | 94.26 |  | 96.82 |  | 97.11 |  |

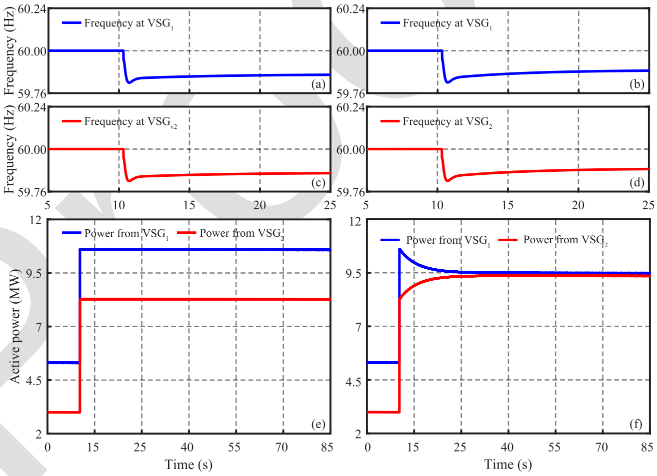

Fig. 5. Impact of droop gain settings on frequency and power sharing: (a) $f_1$ in setting 1, (b) $f_1$ in setting 2, (c) $f_2$ in setting 1, (d) $f_2$ in setting 2, (e) Active power outputs in setting 1, and (f) Active power outputs in setting 2.

Furthermore, the dynamic frequency performance is examined under two droop control configurations for the PFGs embedded in the two GFMI-based BESSs. A 10 MW load pick-up event is applied at a random location within the merged MG. In setting 1, the droop gains are identical $(K_1^{f-p} = K_2^{f-p})$, while in setting 2, the droop gains are different $(3K_1^{f-p} = 2\,K_2^{f-p})$. The corresponding simulation results are illustrated in Fig. 5(a)–(f).

As observed in Fig. 5(a)–(d), the frequency responses of the two BESSs are identical under each setting and are determined primarily by the system-level load imbalance. In setting 1, where both droop gains and VSG parameters are matched, the two BESSs also share active power equally, as shown in Fig. 5(e). However, in setting 2, with unequal droop gains, both BESSs initially contribute equally due to identical damping parameters that dominate the early-stage dynamics. Over time, the final active power sharing is governed by the slower dynamics of the PFG, resulting in an uneven steady-state allocation, as illustrated in Fig. 5(f).

### B. Case 2: Risk-Averse Allocation Results

The stochastic SDMG-BS resource allocation model is solved using the 16 scenarios described in Section IV-B, and the resulting risk-averse allocation is summarized in Table III.

As shown in Table III, the stochastic optimization selects three candidate bus blocks, $\mathrm{B}_2$, $\mathrm{B}_5$, and $\mathrm{B}_8$, to host the GFMI-based BESSs. According to the BESS placement constraint in (13),

TABLE III
RISK-AVERSE RESOURCE ALLOCATION RESULTS

| Resource | Location | Power (MW) | Capacity (MWh) |
|---|---|---|---|
| BESS | Bus 18 | 2.294 | 3.942 |
| BESS | Bus 62 | 1.283 | 2.471 |
| BESS | Bus 98 | 2.222 | 3.587 |
| SSW | Branch (151, 300) | / | / |
| SSW | Branch (60, 160) | / | / |
| SSW | Branch (150, 149) | / | / |

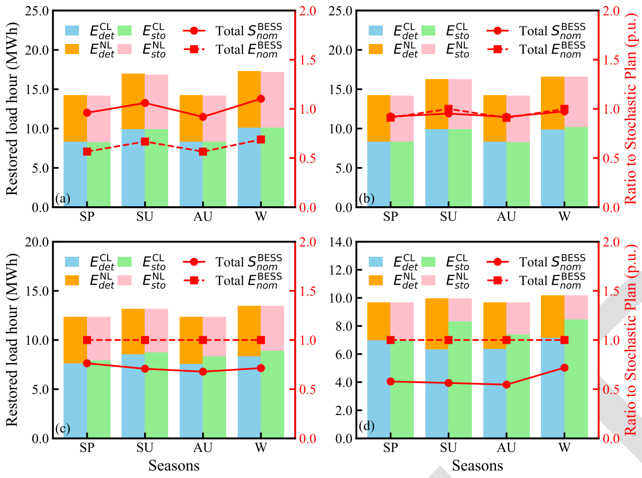

Fig. 6. Comparison between the deterministic and stochastic resource allocation plans under different TG outage durations: (a) 60 minutes, (b) 120 minutes, (c) 180 minutes, and (d) 240 minutes.

each selected bus block includes only one three-phase bus, at which a BESS is sited to form an MG. The chosen buses (18, 62, and 98) lie at the boundaries of their respective blocks, ensuring efficient access to adjacent de-energized segments while minimizing power flow losses.

The rated power and energy capacities of these BESSs are jointly optimized across all scenarios to balance resilience and cost under uncertainty. In addition, the existing ESWs at branches (151, 300), (60, 160), and (150, 149) are upgraded to SSWs, enabling flexible, location-independent synchronization of MGs during the BS process.

Furthermore, the restored critical load $E^{\mathrm{CL}}$ and non-critical load $E^{\mathrm{NL}}$ from 8:45 to 13:45in 15-minutes intervals, obtained using both deterministic and stochastic methods across all scenarios, are illustrated in Fig. 6. The left black y-axis indicates the amount of restored load, while the right red y-axis shows the ratio of the total allocated rated power and energy capacity of each deterministic plan to the stochastic plan.

As seen in Fig. 6(a) and (b), for shorter TG outage durations (60 and 120 minutes), the total allocated rated power in the deterministic plans exceeds that of the stochastic plan (ratios $> 1$), while their allocated capacities are less than or equal to those of the stochastic plan. In these cases, deterministic plans tend to allocate more rated power, potentially over-investing in short bursts of supply, whereas the stochastic plan conserves investment by moderately sizing rated power and re-allocates the saved budget to increase BESS energy capacity, thereby maintaining equivalent load restoration.

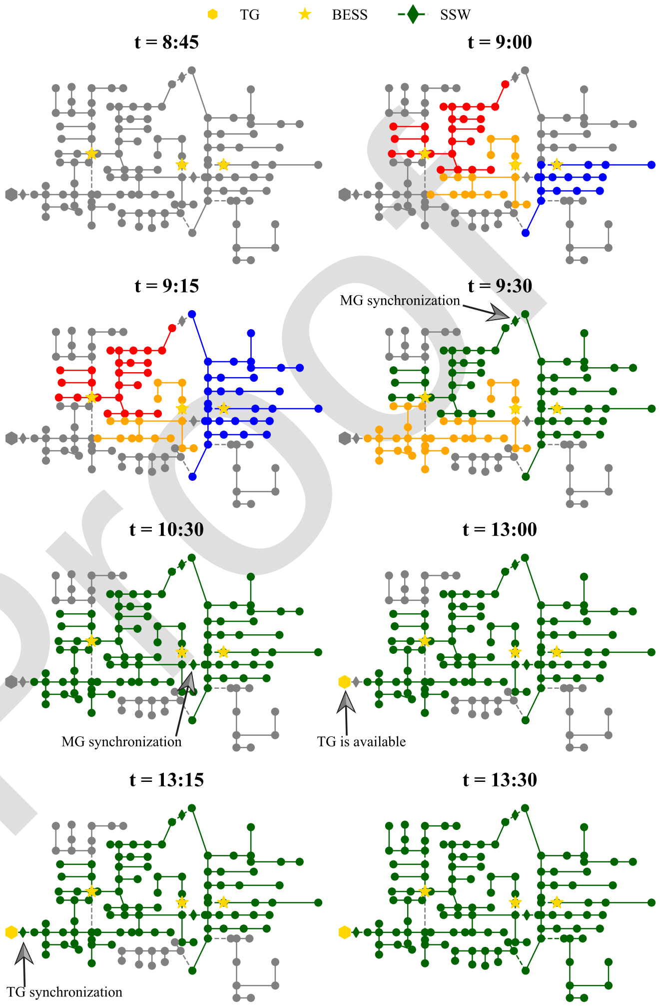

Fig. 7. Optimal BS cranking path of IEEE 123-node feeder under the extreme scenario.

In contrast, for longer TG outage durations (180 and 240 minutes), as shown in Fig. 6(c) and (d), the total allocated capacities of the deterministic plans match those of the stochastic plan (ratios $\approx 1$), but their allocated rated power are noticeably smaller (ratios $< 1$). This outcome reflects the myopic nature of deterministic methods, which fail to anticipate sustained power demands under uncertainty. In comparison, the stochastic plan, by accounting for a wide range of scenarios, achieves significantly better restoration performance. For example, under a 240-minute outage with a summer DER and load profiles, the stochastic plan restores approximately 2MWh more critical load, representing a 20% improvement over the deterministic plan.

### C. Case 3: Optimal BS Process Under Extreme Scenario

The optimal BS process obtained using the stochastic plan for the worst-case scenario (restoring in winter with 240 mins TG outage duration) is shown in Fig. 7. Restoration begins at 8:45 and ends at 13:45, with updates at 15-minute intervals.

As depicted in Fig. 7, without employing the SDMG-BS framework, the DS would have remained without power until

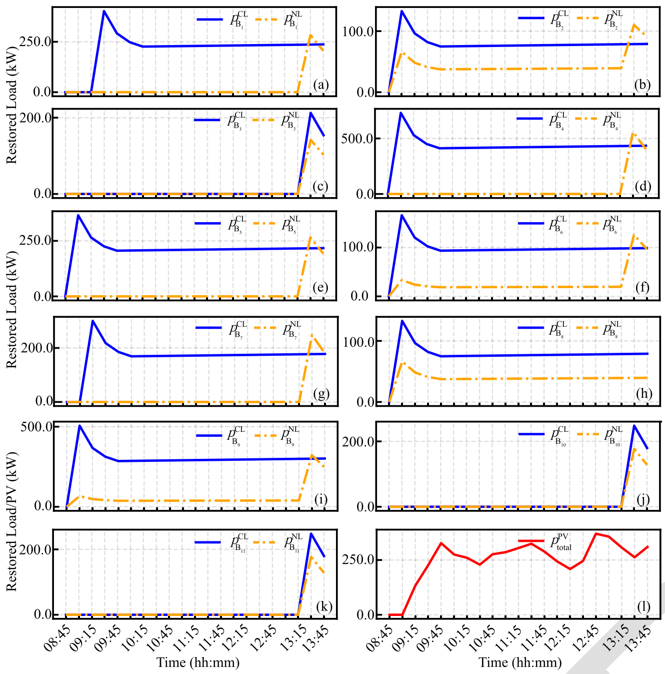

Fig. 8. Restored load in each segment and PV output over time.

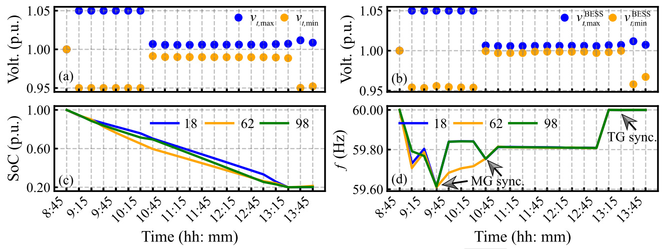

Fig. 9. System performance. (a) Sytem nodal voltage level. (b) BESS nodal voltage level. (c) SoCs of the BESSs. (d) Frequencies of the BESSs.

13:00 due to the loss of TG. However, as shown in Fig. 7, with GFMI capability, BS was initiated at 8:45 by activating GFMIs-based BESSs at bus 18, 62, and 98, represented with gold stars. These BESSs served as the starting points for cranking paths to energize other GFLIs-based behind-meter PVs. By 9:00, the segments containing the BESSs, $B_2$, $B_5$, and $B_8$, and their corresponding nearby segments, $B_4$, $B_6$, and $B_9$, were energized to separately form three isolated MGs, colored as red, orange, and blue, respectively, through closing ESWs (18, 135), (60, 62), and (97, 98). Then, the MG dominated by the BESS at bus 98 expanded its boundary by energizing the $B_7$ through closing ESW (97, 197) until 9:15. At 9:30, the two MGs, ruled by the BESSs at bus 18 and 98 and colored as green, were synchronized by closing the SSW (151, 300), increasing the system's energy and power capacity to restore more PVs and loads. Meanwhile, the $B_1$ was restored by the MG governed by the BESS at bus 62 through acting the ESW (13, 152). One hour later, this MG was synchronized with those two merged MGs by closing the SSW (60, 160), where the GFMI and GFLI resources were shared to maintain the restored segments. This configuration remained in place until 13:00 when the TG returned online and turned its color from grey into gold. However, it wasn't connected until 13:15. At that point, the restored island MG was synchronized with the TG, which picked up the outage $B_3$, $B_{10}$, and $B_{11}$ at 13:30 and realized the final configuration capable of operating continuously moving forward.

The detailed critical and non-critical load restoration profiles segment by segment and the total restored PV output are shown in Fig. 8.

As shown in Fig. 8, the restored load within each segment initially surges above its nominal level due to the CLPU effect, then gradually settles to its normal value over several time steps. Furthermore, because of the prolonged outage in this extreme scenario, only a few bus blocks are able to pick up their non-critical loads during the early stages of restoration, while the majority remain de-energized until the TG becomes available and is reconnected.

The system performances during the BS process are displayed in Fig. 9.

The maximum and minimum nodal voltages at each time step–across all buses and BESSs shown in Fig. 9(a) and (b)–are maintained within the permissible operating range of 0.95 to 1.05 per unit, as enforced by (34c). Similarly, Each BESS's SoC and frequency during the BS process are constrained according to (27b) and (29d), respectively.

Moreover, the synchronization events among restored MGs and with the TG are visualized in Fig. 9(d) through the intersection points of their frequency trajectories. At 9:30, the MG formed by the GFMI-based BESS at bus 18 is synchronized with the MG formed by the GFMI-based BESS at bus 62, with both frequencies converging to approximately 59.61 Hz–within the acceptable threshold. Similiarly, the MG initiated by the GFMI-based BESS at bus 98 synchronizes with the previously merged MG at 10:30, where both frequencies are near 59.75 Hz. Finally, the upstream TG becomes available at 13:00 and is successfully synchronized with the formed MG at 13:15, after which this configuration is maintained for the remainder of the process.

## D. Case 4: Sensitivity Analysis

Given the resource allocation plan obtained from the proposed two-stage stochastic optimization model, where the MGs formed by the BESSs at buses 18, 98, 62 are denoted as $MG_1$, $MG_2$, and $MG_3$, respectively, the dynamic formation processes of these networked MGs under different seasonal DER output profiles, assuming a fixed TG outage duration of 240 minutes, are illustrated in Fig. 10(a)–(d).

As seen in Fig. 10(b)–(d), the MG formation processes under the summer and autumn DER output profiles progress more rapidly than in the winter case, with all three isolated MGs successfully synchronized into a single integrated MG by 9:45. This observation suggests that higher DER output tends to accelerate the restoration process by allowing individual GFMI-based BESSs to energize nearby segments more quickly and synchronize with other MGs through SSWs.

Interestingly, despite the favorable PV output in spring, Fig. 10(a) shows a comparatively slower MG merging process. This delay is primarily attributed to increased load demand and

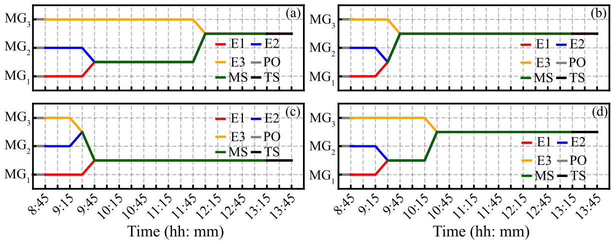

Fig. 10. Dynamic MG formations in: (a) Spring, (b) Summer, (c) Autumn, and (d) Winter. (E1: Energized MG$_1$, E2: Energized MG$_2$, E3: Energized MG$_3$, PO: Power outage, MS: MG synchronization, TS: TG synchronization.).

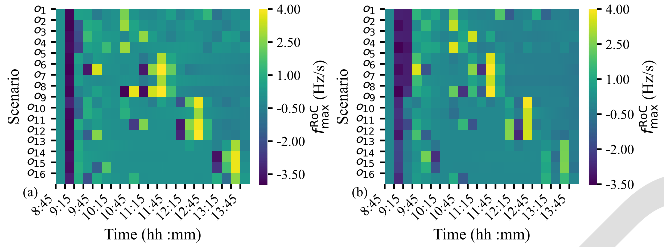

Fig. 11. Maximum RoCoF across all scenarios: (a) MG$_3$, and (b) MG$_2$.

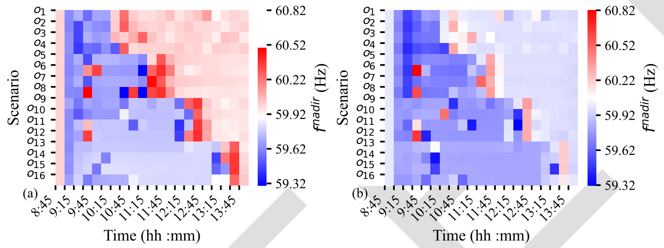

Fig. 12. Frequency nadir across all scenarios: (a) MG$_3$, and (b) MG$_2$.

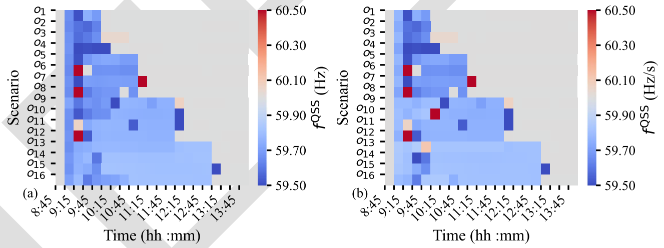

Fig. 13. QSS Frequency across all scenarios: (a) MG$_3$, and (b) MG$_2$.

the associated CLPU effects, which impose additional frequency and power constraints that limit the timing and feasibility of MG synchronization.

The dynamic frequency indices during the BS process under the stochastic resource allocation plan across all deterministic scenarios are presented in Figs. 11–13.

As shown in Fig. 11, negative peaks in the maximum RoCoF (represented by darker blues) predominantly occur during load pick-up events, reflecting the abrupt increase in system inertia demands. These frequency dips are mitigated in scenarios with higher DER outputs, which show RoCoF values closer to zero. Conversely, positive maximum RoCoF spikes (depicted as bright yellow regions) are observed during TG synchronization events, when GFIM-based BESSs reduce their active power support roles. After synchronization with the TG, the RoCoF values stabilize around zero. Across all scenarios, the maximum RoCoF remains within the acceptable operational bounds of $(-4.00 \sim 4.00)$ Hz/s.

Fig. 12 shows that the frequency nadir values follows a similar pattern. More severe frequency dips (represented by deeper blue tones) appear during load pick-up events, particularly in scenarios with limited DER support. In contrast, scenarios with higher DER availability maintain higher nadir values, reducing the risk of frequency instability for GFMI-based BESSs. TG synchronization events lead to slight frequency surges; however, all frequency nadirs remain within the secure operating range of $(57.80 \sim 61.80)$ Hz.

As defined by (7), the QSS frequency is sufficient to capture the operational frequency behavior of the system. Fig. 13 illustrates that the QSS frequencies of MG$_2$ and MG$_3$ remain stable and distinct during their isolated operation phases, always within the acceptable range of $(59.50 \sim 60.50)$ Hz. Once the MGs are synchronized, for instance, between 10:30 to 13:15in Scenario 16, their QSS frequencies converge. After the integrated MG is reconnected with the TG, the frequency stabilizes at the nominal 60Hz, as shown by the consistent light sky-blue region across all scenarios.

## VI. CONCLUSION

This paper proposes a two-stage stochastic resource allocation model with embedded frequency constraints to support the synchronizing dynamic microgrids for black start (SDMG-BS) framework, aimed at restoring DER-dominated DSs following prolonged outages. The model incorporates multiple sources of uncertainties, including seasonal variations in RES output and load demand, as well as varing TG outage durations. To facilitate flexible and adaptive restoration strategies, the SDMG-BS framework enables location-independent synchronization among restored MGs and the TG, coordinated through the operation of SSWs. Frequency security is maintained throughout the BS process via VSG-controlled GFMIs. The key findings are summarized as follows. First, the stochastic allocation strategy acheves more resilient and cost-efficient restoration under uncertain conditions, with up to 20 % additional critical load restored compared to deterministic baselines. Second, the restoration process is initiated from multiple locations by forming islanded MGs, which subsequently coordinate and merge through flexible synchronization enabled by upgraded SSWs. Specifically, two MG synchronization events are executed prior to reconnection with the TG, forming an integrated MG to enhance grid support. Moreover, frequency stability is ensured by constraining transient indices, such as maximum RoCoF, frequency nadir, and QSS frequency, within acceptable limits across all scenarios. The accuracy of the linear frequency model is validated to exceed 90 %, confirming its suitability for long-term planning. Future work will extend the proposed framework to incorporate the dynamic behavior of rotating loads and evaluate the interactions between restoration strategies and distribution-level protection systems.

## APPENDIX A
## VOLTAGE CONTROLLER DEVIATION OF VSG

Terminal voltage of GFMI deviating from the base value ($V^b$) with reactive power output ($q$) and voltage droop gain ($K^{V-q}$) is expressed as follows:

$$V = V^b - K^{V-q}q \tag{45}$$

Given that $v = V^2$ and substituting $V$ into Eq. 45, we get:

$$\begin{aligned} v &= (V^b - K^{V-q}q)^2 \\ &= (V^b)^2 - 2V^b K^{V-q} q + (K^{V-q}q)^2 \\ &= (V^b)^2 + \Delta v^{inc}. \end{aligned} \tag{46}$$

Here, a new variable $v^{inc}$ representing two non-linear terms is introduced for brevity.

## REFERENCES

[1] C. Avraam, L. Ceferino, and Y. Dvorkin, “Operational and economy-wide impacts of compound cyber-attacks and extreme weather events on electric power networks,” *Appl. Energy*, vol. 349, 2023, Art. no. 121577.

[2] S. Konar and A.K. Srivastava, “MPC-based black start and restoration for resilient DER-Rich electric distribution system,” *IEEE Access*, vol. 11, pp. 69177–69189, 2023.

[3] Z. Wang and J. Wang, “Self-healing resilient distribution systems based on sectionalization into microgrids,” *IEEE Trans. Power Syst.*, vol. 30, no. 6, pp. 3139–3149, Nov. 2015.

[4] A. Heidari-Akhijahani and K. L. Butler-Purry, “Black-start service restoration of unbalanced distribution systems considering frequency stability constraints,” in *Proc. 2023 IEEE Power Energy Soc. Gen. Meeting*, 2023, pp. 1–5.

[5] Q. Zhang, Z. Ma, Y. Zhu, and Z. Wang, “A two-level simulation-assisted sequential distribution system restoration model with frequency dynamics constraints,” *IEEE Trans. Smart Grid*, vol. 12, no. 5, pp. 3835–3846, Sep. 2021.

[6] Z. Qin, Y. Li, X. Chen, and H. Liu, “System restoration for low-inertia power systems incorporating fast frequency response via distributionally robust optimization,” in*IEEE Trans. Power Syst.*, vol. 40, no. 3, pp. 2230–2243, May 2025.

[7] T. Ding, Z. Wang, M. Qu, Z. Wang, and M. Shahidehpour, “A sequential black-start restoration model for resilient active distribution networks,” *IEEE Trans. Power Syst.*, vol. 37, no. 4, pp. 3133–3136, Jul. 2022.

[8] Y. Du, H. Tu, X. Lu, J. Wang, and S. Lukic, “Black-start and service restoration in resilient distribution systems with dynamic microgrids,” in*IEEE Trans. Emerg. Sel. Topics Power Electron.*, vol. 10, no. 4, pp. 3975–3986, Aug. 2022.

[9] C. Wang et al., “Frequency-constrained optimal restoration scheduling in active distribution networks with dynamic boundaries for networked microgrids,” in*IEEE Trans. Power Syst.*, vol. 40, no. 3, pp. 2061–2077, May 2025.

[10] F. Yao, T. K. Chau, X. Zhang, H.H.-C. Iu, and T. Fernando, “An integrated transmission expansion and sectionalizing-based black start allocation of bess planning strategy for enhanced power grid resilience,” *IEEE Access*, vol. 8, pp. 148968–148979, 2020.

[11] F. Qiu, J. Wang, C. Chen, and J. Tong, “Optimal black start resource allocation,” *IEEE Trans. Power Syst.*, vol. 31, no. 3, pp. 2493–2494, May 2016.

[12] G. Patsakis, D. Rajan, I. Aravena, J. Rios, and S. Oren, “Optimal black start allocation for power system restoration,” *IEEE Trans. Power Syst.*, vol. 33, no. 6, pp. 6766–6776, Nov. 2018.

[13] B. Zhang, P. Dehghanian, and M. Kezunovic, “Optimal allocation of PV generation and battery storage for enhanced resilience,” *IEEE Trans. Smart Grid*, vol. 10, no. 1, pp. 535–545, Jan. 2019.

[14] Z. Wang, B. Chen, J. Wang, M. M. Begovic, and C. Chen, “Coordinated energy management of networked microgrids in distribution systems,” *IEEE Trans. Smart Grid*, vol. 6, no. 1, pp. 45–53, Jan. 2015.

[15] Y. Du, X. Lu, H. Tu, J. Wang, and S. Lukic, “Dynamic microgrids with self-organized grid-forming inverters in unbalanced distribution feeders,” *IEEE Trans. Emerg. Sel. Topics Power Electron.*, vol. 8, no. 2, pp. 1097–1107, Jun. 2020.

[16] X. Wu, J. Liu, Y. Men, B. Chen, and X. Lu, “Optimal energy storage system and smart switch placement in dynamic microgrids with applications to marine energy integration,” *IEEE Trans. Sustain. Energy*, vol. 14, no. 2, pp. 1205–1216, Apr. 2023.

[17] A. P. Asensio, S. A. Gómez, and J. L. Rodriguez-Amenedo, “Black-start capability of PV power plants through a grid-forming control based on reactive power synchronization,” *Int. J. Elect. Power Energy Syst.*, vol. 146, 2023, Art. no. 108730.

[18] A. Alassi, Z. Feng, K. Ahmed, M. Syed, A. Egea-Alvarez, and C. Foote, “Grid-forming VSM control for black-start applications with experimental phil validation,” *Int. J. Elect. Power Energy Syst.*, vol. 151, 2023, Art. no. 109119.

[19] Y. Zhao, Z. Lin, Y. Ding, Y. Liu, L. Sun, and Y. Yan, “A model predictive control based generator start-up optimization strategy for restoration with microgrids as black-start resources,” *IEEE Trans. Power Syst.*, vol. 33, no. 6, pp. 7189–7203, Nov. 2018.

[20] K. Zou, G. Mohy-ud din, A. P. Agalgaonkar, K. M. Muttaqi, and S. Perera, “Distribution system restoration with renewable resources for reliability improvement under system uncertainties,” *IEEE Trans. Ind. Electron.*, vol. 67, no. 10, pp. 8438–8449, Oct. 2020.

[21] L. Liu, Z. Hu, Y. Wen, and Y. Ma, “Modeling of frequency security constraints and quantification of frequency control reserve capacities for unit commitment,” *IEEE Trans. Power Syst.*, vol. 39, no. 1, pp. 2080–2092, Jan. 2024.

[22] Z. Zhang, M. Zhou, Z. Wu, S. Liu, Z. Guo, and G. Li, “A frequency security constrained scheduling approach considering wind farm providing frequency support and reserve,” *IEEE Trans. Sustain. Energy*, vol. 13, no. 2, pp. 1086–1100, Apr. 2022.

[23] S. Maharjan, C. Bai, H. Wang, Y. Yao, F. Ding, and Z. Wang, “Distribution system blackstart and restoration using DERs and dynamically formed microgrids,” *IEEE Trans. Smart Grid*, vol. 16, no. 3, pp. 2100–2114, May 2025.

[24] Y. L. Li, W. Sun, W. Yin, S. Lei, and Y. Hou, “Restoration strategy for active distribution systems considering endogenous uncertainty in cold load pickup,” *IEEE Trans. Smart Grid*, vol. 13, no. 4, pp. 2690–2702, Jul. 2022.

[25] *IEEE Standard for Interconnection and Interoperability of Distributed Energy Resources With Associated Electric Power Systems Interfaces*, IEEE Standard 1547-2018, Apr. 2018.

[26] C. Utama, C. Meske, J. Schneider, and C. Ulbrich, “Reactive power control in photovoltaic systems through (explainable) artificial intelligence,” *Appl. Energy*, vol. 328, 2022, Art. no. 120004.

[27] R. Cheng, Z. Wang, Y. Guo, and Q. Zhang, “Online voltage control for unbalanced distribution networks using projected Newton method,” *IEEE Trans. Power Syst.*, vol. 37, no. 6, pp. 4747–4760, Nov. 2022.

**Cong Bai** (Graduate Student Member, IEEE) received the B.S. degree in electrical engineering and its automation from the Kunming University of Science and Technology, Kunming, China, in 2020, and the M.S. degree in electrical engineering from Chongqing University, Chongqing, China, in 2023. He is currently working toward the Ph.D. degree with the Department of Electrical & Computer Engineering, Iowa State University, Ames, IA, USA. His current research interests include power system restoration, inverter-based resource integration, control and optimization of distribution systems.

**Salish Maharjan** (Member, IEEE) received the Ph.D. degree in electrical and computer engineering from the National University of Singapore, Singapore, in 2020. He was a Visiting Student with the Massachusetts Institute of Technology, Cambridge, MA, USA, in 2014. He is currently a Research Assistant Professor with the Department of Electrical & Computer Engineering, Iowa State University, Ames, IA, USA. His research interests include distribution system modeling, stability analysis, optimization and control for techno-economic operation, and resilience enhancement. He was the recipient of the Best Paper Award at 2023 IEEE Power & Energy General Meeting.

**Han Wang** received the B.Sc. degree in new energy science and engineering from the Chinese University of Hong Kong, Shenzhen, China, in 2019, and the Ph.D. degree in electronic and electrical engineering from the University of Leeds, Leeds, U.K., in 2023. He is currently a Postdoctoral Research Associate with the Department of Electrical & Computer Engineering, Iowa State University, Ames, IA, USA. His research interests include electric vehicle charging analysis and control, electricity market, power system resilience, artificial intelligence applications in power systems, and power system optimization.

**Zhaoyu Wang** (Senior Member, IEEE) received the B.S. and M.S. degrees in electrical engineering from Shanghai Jiao Tong University, Shanghai, China, and the M.S. and Ph.D. degrees in electrical and computer engineering from the Georgia Institute of Technology, Atlanta, GA, USA. Since 2015, he has been an Assistant, Associate, and Full Professor with Iowa State University, Ames, IA, USA. His research interests include optimization and data analytics in power distribution systems and microgrids. He was the recipient of the National Science Foundation CAREER Award, IEEE Power and Energy Society (PES) Outstanding Young Engineer Award, ISU Award for Mid-Career Achievement in Research, Northrop Grumman Endowment, ISU College of Engineering's Early Achievement in Research Award, and the Harpole-Pentair Young Faculty Award Endowment. He is the Lead Principal Investigator for more than $24 M projects funded by the National Science Foundation, the Department of Energy, National Laboratories, PSERC, and Iowa Economic Development Authority. He is the Secretary and Technical Committee Program Chair of IEEE Power System Operation, Planning and Economics Committee, the Vice Chair of IEEE Distribution System Operation and Planning Subcommittee, the Secretary of IEEE Task Force on IEEE P3102 Standard for Conservation Voltage Reduction Data Collection and Management Procedures, and the Chair of IEEE Task Force on Advances in Natural Disaster Mitigation Methods. He is an Associate Editor for IEEE TRANSACTIONS ON SUSTAINABLE ENERGY, IEEE OPEN ACCESS JOURNAL OF POWER AND ENERGY, IEEE POWER ENGINEERING LETTERS, and *IET Smart Grid*. He was an Associate Editor for IEEE TRANSACTIONS ON POWER SYSTEMS and IEEE TRANSACTIONS ON SMART GRID. Dr. Wang is an IEEE PES Distinguished Lecturer.